

Temporal and spatial evolution of soil surface roughness on stony plots

Li Li^{a,*}, Mark A. Nearing^b, Mary H. Nichols^b, Viktor O. Polyakov^b, C. Larrabee Winter^c, Michelle L. Cavanaugh^b

^a School of Natural Resources and the Environment, University of Arizona, Tucson, AZ, 85705, USA

^b USDA-Agricultural Research Service, Southwest Watershed Research Center, Tucson, AZ, 85719, USA

^c Department of Hydrology and Water Resources, University of Arizona, Tucson, AZ, 85721, USA

ARTICLE INFO

Keywords:

LiDAR
Soil surface roughness
Rock cover
Random roughness
Fractal dimension
Multifractal analysis

ABSTRACT

Soil surface roughness (SSR) is widely recognized as an important factor influencing water erosion processes. On semiarid hillslopes with stony soils, rock fragments accumulate as the result of preferential erosion of fine materials, often creating a rough, rocky surface. A series of rainfall events were simulated on a stony plot (2 × 6.1 m) at three slope gradients (5 %, 12 %, and 20 %) and rock cover was measured. Surface elevations were sampled by terrestrial LiDAR at high resolutions. Roughness indices, including random roughness (RR), fractal dimension, crossover length, and generalized fractal dimension, were calculated from LiDAR points directly. Results showed: 1) SSR displayed an increasing trend as the rainfall simulation proceeded for all three slope treatments; 2) the steeper slope developed greater surface roughness; and 3) both the increase of surficial exposed rocks and the formation of erosional features, e.g., rills and depressions, contributed to the spatio-temporal variations of SSR. Results also showed that the fractal dimension was not a good indicator of soil surface roughness, but rather was an index of the form of the surface. Crossover length was a measure of roughness at a scale of a few millimeters, while random roughness was a measure of elevation variations on the scale of the length of the transect measured, and thus encompassed larger morphological features including rills. We also established a new method for multifractal analysis that characterized the heterogeneity of soil surface roughness. These results improve our understanding of the evolution of semiarid stony hillslopes and the dynamic feedback mechanism between erosion, surface morphology and hydraulics.

1. Introduction

Soil surface roughness (SSR) describes the small-scale elevation irregularity or undulation magnitudes of the soil surface and is often related to many hydrologic and erosion processes (Govers et al., 2000; Bauer et al., 2015). Four distinct types of surface roughness, including micro-relief variation, random roughness, oriented roughness and high order roughness, were classified by Römkens and Wang (1986) according to the magnitudes of roughness elements (from few millimeters to several meters) or factors that contributed to the roughness (from soil grains to landscape features). Most past research has focused on soil random roughness at the scale of approximately 2–200 mm (Darboux et al., 2001; Helming et al., 1993; Huang and Bradford, 1992; Römkens and Wang, 1986; Vermang et al., 2015). Previous studies have shown that SSR affects both the hydrologic behaviors and functions of water flow (Darboux et al., 2001), as for example, runoff generation and sediment production (Gómez and Nearing, 2005; Zhao et al., 2016; Ding and Huang, 2017), leading to the inclusions of SSR in many process-

based hydrologic and erosion models. Dynamic erosion continuously creates and alters the SSR. Consequently, the modified SSR will in turn dynamically change the erosion patterns. Hence, the temporal variation of SSR is not only a descriptor that reflects how the soil surface behaves against the erosive agents (Huang and Bradford, 1992), but also a potential index to distinguish different erosion stages (Huihui et al., 2016). It is therefore important to understand the dynamic temporal and spatial evolution of SSR due to water erosion.

Spatial and temporal SSR variations have been widely discussed, and rainfall is recognized as one of the major factors that contribute to the spatiotemporal variations (Darboux et al., 2001; Helming et al., 1993). Soil surfaces may display a decline in SSR over time due to the breakdown of aggregates and subsequent sealing of the surface (Huang and Bradford, 1992; Vermang et al., 2013; Van Wesemael et al., 1996), while increased SSR trends may also exist associated with the development of erosional features, such as rills or headcuts (Govers, 1992; Huang, 1998; Huang and Bradford, 1992; Lei et al., 1998). The above results generally come from experimental soils without rock fragments,

* Corresponding author at: 2000 E Allen Road, Tucson, AZ, 85719, USA.

E-mail address: lili2@email.arizona.edu (L. Li).

where soil structure and erosional features are dominant factors that determine SSR.

On semiarid hillslopes, abundant rock fragments are found on the soil surface as a result of selective erosion (Abrahams et al., 1994; Polyakov et al., 2018). Erosion pavement is a result of hillslope evolution process that defined by Shaw (1929) as “a surface covering of stone, gravel, or coarse soil particles accumulated as the residue left after sheet or rill erosion has removed the finer soil”. Once erosion pavement develops, the accumulated rock fragments may increase the SSR by pedestalling or protruding from the surface, which is unlike the case of soil aggregates that generally experience breakdown during rainfall and subsequent reduction in surface roughness (Van Wesemael et al., 1996). Erosion-induced increasing SSR is expected to impose greater resistance to flow velocities, and hence reduce the erosion potential and change the erosional patterns. The dynamic feedback between the erosion and its induced rock pavement may challenge some frequently used assumptions, e.g., a transport-limited sediment transport model (Willgoose and Sharmeen, 2006) and slope gradient-dependent velocity relationships such as Chezy and Manning equation (Govers, 1992; Nearing et al., 2017). Insights into those dynamic interactions and characterizations of the evolution of semiarid stony hillslopes require an understanding of the evolution of surface morphological characteristics (Willgoose and Sharmeen, 2006). However, few studies of the evolution of SSR on stony surfaces have been reported. Van Wesemael et al. (1996) simulated rainfall on 13 simulated plow layers with different initial soil moisture contents, rock fragment contents, and sizes to investigate the SSR variations over multiple rainfalls. However, the total applied rainfall volume (192.5 mm), which was of the order of the annual precipitation in southeastern Spain, was insufficient to account for the long-term effects of rainfall on SSR.

Nearing et al. (2005) hypothesized that through the process of preferential erosion the surface physical roughness of stony hillslopes with different slope gradients might evolve in such a way that steeper areas develop a relative increase both in physical and hydraulic roughness. In the study of Nearing et al. (2005), the estimated spatial erosion rates in two stony, semiarid watersheds using ^{137}Cs inventories were shown to not be a function of hillslope steepness or curvature, but rather a function of rock content of the surface soil. They further speculated that these results were due to the different surface hydraulic and physical roughness levels induced by the historical erosion that resulted in rougher surfaces due to greater preferential erosion on steeper slopes. In the hypothesis testing experiment of Nearing et al. (2017), 22 rainfall events were simulated on stony plots (2 by 6.1 m) with three slope treatments (20 %, 12 % and 5 %, two replications for each slope treatment). The total applied rainfall volume for each surface replication ranged from 1400 to 2240 mm, at relatively high intensity, to account for medium-term (ca. 10 years) rainfall erosion effects. Surface elevations were measured by a laser device along three transects that crossed the plots for assessing SSR using the random roughness index, and rock covers were measured using a pointer method at 300 points on a 20 by 20 cm grid. The results showed that final random roughness was positively correlated with slope gradient, even though the final rock cover was similar at the different slopes. Their study investigated the evolution of stony surfaces in a systematic way, and the results enhanced the understanding of temporal variations of SSR on stony hillslopes. However, given the limited transect measurements in their study, interpretation of the experiment would benefit from denser surface elevation measurements and multiple roughness indices for describing the spatiotemporal variations of SSR.

The objective of the present research is to investigate the spatio-temporal SSR evolution of stony plots under simulated rainfall with highly dense surface elevation measurements and multiple roughness indices based on the soil surface spatial properties. Terrestrial LiDAR scanning (TLS) measurements were conducted to sample the soil surface morphology at high resolutions in the rainfall simulation experiments of Nearing et al. (2017). Random roughness indices and fractal

parameters were employed to investigate how the SSR of stony soils responded to the simulated rainfalls. In order to investigate the soil surface complexity in a thorough way, multifractal analyses with the use of a new probability function were also conducted. The results of the study show the benefits of using a variety of roughness and form parameters to best characterize surfaces and changes in surface as a function of erosion.

2. Background

2.1. Random roughness

One of the most frequently employed SSR indices is random roughness. RR was first proposed by Allmaras et al. (1966) as the standard error of log-transformed elevation measurements, after the slope and tillage effects were removed. However, the log transformation was found not to be necessary (Currence and Lovely, 1970). In the present study, the standard deviation of elevation measurements was calculated as random roughness, similar as in Vermang et al. (2013) and others:

$$RR = \sqrt{\frac{1}{N} \sum_{j=1}^N [Z_j - \bar{Z}]^2} \quad (1)$$

Where, Z_j is the elevation measurement at point j , N is the number of the measurements, and \bar{Z} is the average value of those N measurements.

2.2. Fractal analysis

One of the drawbacks of random roughness index is its inability to account for spatial and geometric properties of surface microtopography (Vermang et al., 2013), therefore, substantial effort has been devoted to quantifying the fractal nature of the surface roughness. The most frequently used structure functions for assessing the fractal dimension are semivariance functions (Darboux et al., 2001; Huang and Bradford, 1992) and root mean squares (RMS) (Vidal Vázquez et al., 2005, 2006). For very dense elevation measurements, such as for a LiDAR point cloud, however, significant computational effort is required to find the pairs of points within predesigned lag distances among the very dense and unevenly spaced points when a semivariance function is employed, leading to some practical compromises of reducing the original LiDAR point cloud density or selecting smaller patches from areas of interest (Abban et al., 2017; Nouwakpo et al., 2016). The RMS method has advantages compared with semivariance functions in its efficiency in fractal analysis and lower estimation errors (Vidal Vázquez et al., 2005, 2006). More details of the RMS method are given here.

In the RMS method, for a given scale h , the variations from the mean of individual elevation points of each window with the size of h by h are averaged, and then the average value of all of the windows, $W(h)$, is assigned for that scale h . The guiding principle of the RMS method is to estimate the average local roughness, $W(h)$, for various scales as (Vidal Vázquez et al., 2005):

$$W(h) = \frac{1}{N_h} \sum_{u=1}^{N_h} \left\{ \frac{1}{m_u} \sum_{i=1}^{m_u} [Z_i - \bar{Z}]^2 \right\}^{1/2} \quad (2)$$

Where, h is the size of a square window, m_u is the number of points that fall in a particular window, u , with the size of h , Z_i and \bar{Z} are the elevations and average elevation of those m_u points, N_h is the total number of windows with the size of h , and $W(h)$ is the RMS for the scale h .

Fig. 1 shows an idealized plot of $\log(W(h))$ plotted vs. $\log(h)$ for a soil surface. If the soil surface exhibits fractal behavior at the smaller range of scales, then linearity near the origin of $\log(W(h))$ versus $\log(h)$

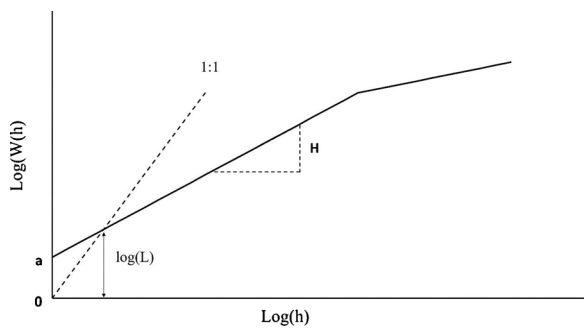


Fig. 1. Idealized schematic for soil surfaces of the logarithm of the RMS local roughness, $W(h)$, as a function of scale, h . H is the Hurst exponent, related to fractal dimension, D , as $D = 3 - H$. The intercept 'a' and Hurst exponent are used to calculate the crossover length, L .

will give an estimation of two important parameters, the Hurst exponent (H) and crossover length (L) (Malinverno, 1990), if using a fractal Brownian motion model (Huang and Bradford, 1992; Vidal Vázquez et al., 2005). The Hurst exponent, H , is simply the slope of the line, representing the rate of change of $\log(W(h))$ with $\log(h)$, which is often linear for soil surfaces at small values of h . Empirically we know that H is greater than zero and less than one for soil surfaces. The crossover length, L , is the parameter that relates the magnitude of the roughness to the magnitude of the scale, h (Brown, 1987). Put another way, L gives dimensionality to the roughness, using the following equation:

$$W(h) = L^{1-H}h^H \quad (3)$$

Note that the units of $W(h)$, h , and L are all length (e.g., mm), H is less than one, and hence by the use of L^{1-H} , both side of the equation have units of length. Note that the crossover length is that value of h where $h = L = W(L)$. Hence L is the "crossover" length where for values less than L , $W(h) > h$ (i.e., roughness is greater than cell size), and for values greater than L , $W(h) < h$. The equation for the straight portions of the graphs in Fig. 1 is:

$$\log[W(h)] = H\log(h) + a \quad (4)$$

Where, a is the intercept, e.g., the value of $\log(W(h))$ at $\log(h) = 0$, e.g., $h = 1$ in whatever units are being used. From Eqs. [3] and [4] it follows that the crossover length may be calculated as:

$$L = \exp\left(\frac{a}{1-H}\right) \quad (5)$$

Fractal dimension, D , for a surface, is defined as

$$D = 3 - H \quad (6)$$

based on the previous studies (Gneiting and Schlather, 2004; Huang and Bradford, 1992). In this scenario, since $0 < H < 1$, soil surfaces will always have fractal dimensions between the values of 2 (a uniform plane) and 3 (a volume), which is consistent with fractal theory. Fractal dimensions characterize the extent to which the object deviates from its topological dimension space towards its embedding dimension space. In this case the deviation is from the planer surface at two dimensions toward filling three-dimensional space.

It is important here to note that both H and D are scale independent parameters. Hence they are expected to be related to the form, and in fact to the complexity (or the irregular geometry, see Wong, 1987), of the surface, but not necessarily to the actual magnitude of the surface elevation variations, and hence to the surface roughness magnitudes. As argued by Kamphorst et al. (2000) that fractal indices are "regression parameters" that describe the form of the variogram (e.g., the semi-variogram and the $W(h)$), instead of a measure of roughness or scale itself. In other words, one can theoretically have two surfaces that have the exact same form, but with very different sizes, that have the same

fractal dimensions. The crossover length, L , is the parameter that provides scale to the form. Referring to Fig. 1, we see that for a given value of D which is a function of H , the value of L indicates the positioning of that line on the graph. Without crossover length, L , it is like defining a straight line on a graph paper without a known intercept. Hence we expect, and others have found (e.g., García-Serrana et al., 2018; Huang and Bradford, 1992; Vidal Vázquez et al., 2005) that the crossover length is related to surface roughness, while fractal dimension is not always so. One might hypothesize that D will be useful for comparing differences in anisotropy, heterogeneity of microtopography, and other morphological differences of soil surfaces.

2.3. Multifractal analysis (MFA)

A single fractal dimension uses a monofractal approach to characterize the complexity of spatial objects (Salat et al., 2017; Martínez et al., 2009), and as introduced above, relies on an averaging process with an assumption that local measurement is self-similar on a limited range of scales (Fig. 1) (Wong, 1987). Multifractal analysis extends this concept by recognizing that, for a given scale, the roughness measurements of the windows with the size of h are spatially varied and can be represented by a probability distribution (Lopes and Betrouni, 2009; Luo et al., 2017). Several studies have shown the soil surface may display multifractal characteristics, and the theory of MFA has been thoroughly described (Luo et al., 2017; Moreno et al., 2008a, b; Martínez et al., 2009; Vidal Vázquez et al., 2010, 2008). Since we created a new way to conduct MFA, the detailed procedures of MFA used in our study are provided in the Method section.

3. Materials and methods

3.1. Soil box preparation

Rainfall was simulated on a 2 m wide by 6.1 m long metal-bound box (Fig. 2). The experimental soil was collected from the top layer (0–15 cm) in the Lucky Hills area located in the Walnut Gulch Experimental Watershed (31° 44' 34"N; 110° 03' 51" W). The soil is classified as Luckyhills-McNeal gravel sandy loam with 52 % sand, 26 % silt, 22 % clay and less than 1 % organic matter (Nearing et al., 2007; Renard et al., 2008). The collected soil was turned over and mixed several times in order to homogenize the materials before filling the box, and subsequently stored in a pile. The slope gradient of the soil box was adjustable, ranging from 0 to 20 %. In the present study, three slope treatments of 20 %, 12 % and 5 % were utilized. Each slope treatment included two replications. Therefore, the present study consisted of six individual experiments in total. For clarity, in this paper "experiment" refers to a single replication of a designated slope gradient. For each



Fig. 2. Photo of the experimental setup.

experiment, the box was positioned horizontally to fill with soil to a depth of 20 cm. The soil surface was then scraped lightly with a wooden block to obtain an even surface.

3.2. Rainfall applications

Rainfall was simulated by a Walnut Gulch Rainfall Simulator (WGRS) (Paige et al., 2003). The WGRS contained a computer-controlled oscillating boom upon which four VeeJet 80100 nozzles spaced 1.52 m apart were mounted. By controlling the spray time of nozzles, various rainfall rates ranging from 13 to 190 mm h⁻¹ with the kinetic energy of approximately 204 kJ ha⁻¹ mm⁻¹ were obtained crossing a 2 by 6.1 m area. Detailed information about the WGRS was presented in Paige et al. (2003). Windscreens were set up around the soil box to minimize unwanted wind disturbances.

For each experiment, the soil surface was first covered with a porous cloth and pre-wet with 35 mm h⁻¹ intensity of rainfall for 30 min. This was done to create consistent initial moisture conditions for each experiment. The box was then adjusted to the designated slope (5 %, 12 %, and 20 %) and the porous cloth was removed.

Rainfall was simulated three times for the 20 % slope and four times for the 12 % and 5 % slope. Each simulation was considered as a single event with continuous rainfall application, and rainfall duration of each simulation varied from 1.5 to 5 h. For each experiment, the first simulation started from low intensity (59 mm h⁻¹) for a period of approximately 20–30 min until steady state runoff was reached and velocity data were collected, and then rainfall was applied for approximately one hour of rainfall at high intensity (178 mm h⁻¹), followed by approximately 15 min at low intensity (59 mm h⁻¹) again. Each subsequent simulation started from high intensity (178 mm h⁻¹) and then decreased to low intensity (59 mm h⁻¹) for variable time lengths depending on how quickly the surface evolved at the various slopes. Detailed descriptions of the rainfall simulation procedures of each experiment were presented in Nearing et al. (2017).

3.3. Surface elevation measurements

The soil surface was scanned prior to the experiment (after pre-wetting) and following each application of rainfall with a RIEGL VZ400¹ terrestrial LiDAR scanner (TLS) (www.riegl.com). This instrument provides high speed and non-contact data acquisition through a collimated beam with a nominal divergence of 0.3 mrad (0.3 mrad corresponds to an increase of 30 mm of beam diameter per 100 m distance) (Riegl GmbH, 2012). Because TLS point density is dependent on the distance of the TLS sensor to the scanned object, soil surfaces far from the scanner were sampled at a lower density than those close to the scanner. Six scan positions were established to sample the soil surface morphology. The scan positions are schematically shown in Fig. 3. At each scan position, the TLS scanner was configured to emit a pulse at 0.04° increments in the azimuth (0–360°) and zenith (30–130°) direction, resulting in approximately one point every 1 mm at a distance of 2 m and every 6 mm at a distance of 8 m. Eight control points were established around the soil box (Fig. 3), and their coordinates were surveyed with a Trimble R8 robotic total station¹. Eight cylindrical reflectors with diameters of 10 cm were set up over the control points on survey tripods. For each experiment, TLS scans were conducted before each simulation and at the end of the last simulation. The details of surface rock cover measurement were available in the study of Nearing et al. (2017).

¹ Trade names and company names, included for the benefit of the reader, do not imply endorsement or preferential treatment of the product listed by the USDA.

3.4. TLS data processing

TLS scans were conducted from six positions to reduce the occlusion effects induced by the rocks and the slope steepness. Scans from different positions needed to be transformed into an external coordinate system from the different internal spherical coordinate systems to obtain a composite point cloud. Scan to scan registrations were accomplished in two steps. First, corresponding reflectors among the scans were matched. In that step, at least three reflectors were required to match the scans. Then the iterative closest point (ICP) (Besl and McKay, 1992) algorithm implemented in the Riegl RiScan Pro¹ software was applied to further register the six scans to obtain a composite TLS point cloud.

To avoid the boundary effects of the soil box borders, approximately 23, 23, 26 and 10 cm of outer edges of left, right, upper and lower of the box, respectively, were cut off from the original composite point cloud, resulting in a TLS point cloud covering an area of 5.63 m by 1.53 m. The slightly different cutoffs of each side were because of the different shadow effects of the metal bounds of soil box. In order to avoid interpolation error and interpolation-induced surface information loss, all the following roughness indices were calculated based on the TLS point clouds directly without converting to DEMs and density reduction.

3.5. Roughness index

3.5.1. Random roughness (RR)

RR was assessed for individual transects rather than the entire plot, as we were interested in the random roughness in different sections (lower, middle, and upper) of the plots. For each surface, a total 560 transects across the plot were identified with an interval of 1 cm and with procedures as follows: 560 straight lines across the plot with 1 cm distance apart were first defined, and each line was treated as the center line of a band with 2 mm width. Each band was then considered as an individual transect. TLS points that fell into each 2 mm wide band were first linearly de-trended to correct for the slope effects and then used for calculating the RR for that band.

3.5.2. Fractal dimension

For each surface, the entire surface was first linearly de-trended to correct for the slope effects. Subsequently, a 1 by 1 cm grid was created to cover the surface, the reason being that in our dataset average point distance was approximately 3 mm and the 1 by 1 cm grid ensured that sufficient number of points are included in the deviation calculations. There were 86,139 cells at $h = 1$ cm on the 5.63 m by 1.53 m area. The window sizes, h , ranged from 2 cm to 100 cm with 1 cm increments, and every possible window on the plot for each of the 99 values of h were considered. In other words, for example, for the $h = 100$ cm grid size, we can start with a 100 cm cell in the upper left side of the plot, then a second 100 cm cell to the right by one cm, and another moved to the right another one cm, and so forth until the right side of the cell reaches the right edge of the plot area. Then we would move back the left of the plot (in terms of the calculations) and down one cm for a second row of cells, and so forth until we reach the bottom of the plot.

$W(h)$ was calculated for each scale, h , using Eq. (2). The calculated $W(h)$ was plotted against h , and linear regression was performed to obtain the slope, H , and hence fractal dimension, D from Eq. (6). The crossover length, L , was calculated using Eq. (5).

3.5.3. Multifractal analysis (MFA)

Since MFA relies on the distribution of local measurements, the fundamental first step to conducting MFA is to establish a probability distribution. The routine step for establishing a probability distribution is to normalize the elevation of each point and use the normalized value as the probability assigned for that point. Thus, the greater the elevation is, the greater the probability is (Luo et al., 2017; Moreno et al., 2008a, b; Martínez et al., 2009; Vidal Vázquez et al., 2008, 2010).

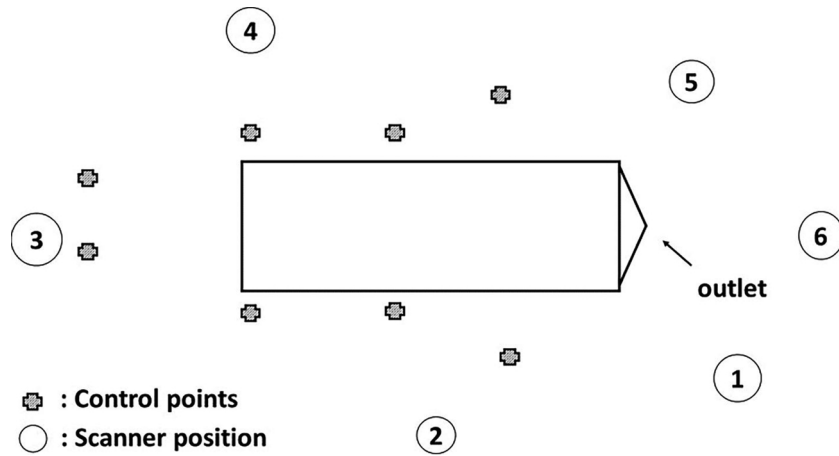


Fig. 3. Relative locations of the six scanning positions and control points. The numbers inside the circles are the ID of scanning positions.

However, that method is not suitable when LiDAR points are utilized directly. When a DEM is used, each cell of the grid has a single elevation point associated with it, and hence equal weighting. The LiDAR points, however, are unevenly spaced, and hence there will be varying numbers of elevation points within each cell, and hence the cells would not be weighted accurately. In this research a new probability measure was established specifically for unevenly spaced points, the procedure of which was:

- (1) The entire surface was first linearly de-trended to remove the slope effect.
- (2) The entire surface was divided into cells with side lengths of $h = 16, 32, 64,$ and 128 mm, with no overlap of cells or plot edges. Therefore, for a given side length of h , the number of $N(h) = \frac{A \times B}{h^2}$ of cells were obtained, where $A = 1536$ mm and $B = 5632$ mm is the width and length of the soil surface.
- (3) For each cell, the measure of that cell was defined as the standard deviation of elevation measurements of points in that cell, S_j . The probability value assigned to a cell was:

$$\mu_j(h) = \frac{S_j}{\sum_i^{N(h)} S_i} \quad (7)$$

Thus, instead of normalizing the elevations, the roughness of each cell was normalized and used as a probability measure. The main consideration here was that standard deviation of elevation measurements of each cell reflected the local roughness measurement that was of interest and avoided the effects of variable numbers of points in each cell.

- (4) The partition function $\chi(q, h)$ was defined as the weighted summation of the q^{th} power of the distribution probability of each cell at the scale h (Vidal Vázquez et al., 2008):

$$\chi(q, h) = \sum_{j=1}^{N(h)} \mu_j(h)^q \quad (8)$$

Different values of the weighting factor, q , provide different types of information about the fractal nature of the surface, as discussed below.

- (5) For each weighting factor, q , the generalized fractal dimension $D(q)$ was calculated based on the following formulas (Vidal Vázquez et al., 2008):

$$D(q) = \frac{1}{q-1} \lim_{h \rightarrow 0} \frac{\ln[\chi(q, h)]}{\ln(h)}, \text{ when } q \neq 1 \quad (9)$$

$$D(q) = \lim_{h \rightarrow 0} \frac{\sum_{j=1}^{N(h)} \mu_j(h) \ln[\mu_j(h)]}{\ln(h)}, \text{ when } q = 1 \quad (10)$$

A log-log plot of $\chi(q, h)$ versus h for each weighting factor, q , tends to be linear if the soil surface of interest has multifractal characteristics (Martínez et al., 2009), and then the fitted linear slope can be used to estimate the generalized fractal dimension $D(q)$ using Eq. [9] and [10]. The coefficients of determination r^2 of the linear fitting may be used for checking whether multifractal characteristics were significant. In the present study, the weighting factor, q , was chosen from -5 to 5 with an increment of 1 .

Both the shape of the $D(q)$ curves and some parameters that are taken or derived from the $D(q)$ function can be used for assessing the degree of heterogeneity of the soil surface. Beside the shape of $D(q)$ vs. q , the following parameters were calculated in the present study:

- (1) $D(0)$. $D(0)$ is the fractal dimension for $q = 0$. Theoretically, if there are no empty cells, then $D(0) = -\frac{\ln(N(h_1)) - \ln(N(h_2))}{\ln(h_1) - \ln(h_2)} = -\frac{\ln\left(\frac{A \times B}{h_1^2}\right) - \ln\left(\frac{A \times B}{h_2^2}\right)}{\ln(h_1) - \ln(h_2)} = 2$. If there are empty cells, $D(0)$ will be less than 2 . Therefore, $D(0)$ is independent of the probability of each cell and only reflects whether the cells are occupied or not and is called the capacity dimension.
- (2) $D(1)$. $D(1)$ is the fractal dimension for $q = 1$ and quantifies the degree of heterogeneity of the distribution by measuring the Shannon entropy, so it is referred to as information dimension (Martínez et al., 2009; Vidal Vázquez et al., 2008). In the case that the $\mu_j(h)$ of each cell is identical, then $D(1) = \lim_{\epsilon \rightarrow 0} \frac{\sum_{j=1}^{N(h)} \mu_j(h) \ln[\mu_j(h)]}{\ln(h)} = \frac{\sum_{j=1}^{N(h_1)} \mu_j(h_1) \ln[\mu_j(h_1)] - \sum_{j=1}^{N(h_2)} \mu_j(h_2) \ln[\mu_j(h_2)]}{\ln(h_1) - \ln(h_2)} = \frac{\frac{AB}{h_1^2} \times \frac{h_1^2}{AB} \times \ln\left(\frac{h_1^2}{AB}\right) - \frac{AB}{h_2^2} \times \frac{h_2^2}{AB} \times \ln\left(\frac{h_2^2}{AB}\right)}{\ln(h_1) - \ln(h_2)} = 2$ which is equivalent to the capacity dimension $D(0)$. Therefore, the closer the $D(1)$ value is to $D(0)$, the more homogeneous is the distribution (Vidal Vázquez et al., 2008).
- (3) ΔD . ΔD is the width parameter, which is the span of the $D(q)$ function and calculated in the present study as $D(q = -5) - D(q = +5)$. It has been suggested as a parameter to describe the variation of a fractal object, which in this case is the variation between cells of the variability of elevations. The greater the ΔD is, the greater complexity the object exhibits (Luo et al., 2017; Roisin, 2007; Vidal Vázquez et al., 2008).
- (4) Multifractality index (MI). MI is defined as $MI = -\Delta(D(0) - D(2))$ by Vidal Vázquez et al. (2008). It is used to minimize the uncertainty of the slope fitting processes. The lower MI is, the greater heterogeneity the surface displays (Vidal Vázquez et al., 2008).

4. Results and discussion

4.1. Random Roughness index

Fig. 4 shows the average RR of the entire plot for replications of the three slope treatments over time. The average RR exhibited an

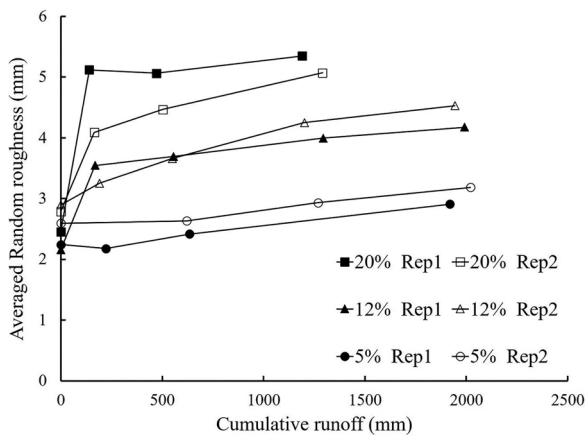


Fig. 4. The averaged random roughness of 560 transects for each surface as functions of the cumulative runoff.

increasing trend as rainfall progressed. The final random roughness values were statistically different among the three slope treatments; the steeper the slope was, the greater the surface roughness was. The average RR values were different from those reported by Nearing et al. (2017), which is attributable to the use of only three transects measurements in his study and the different method (laser distance meter) of measurement used.

4.2. Fractal analysis

4.2.1. The $W(h)$ function

Fig. 5 shows the calculated $W(h)$ against window size, h , for all surfaces. For all the 24 surfaces, $W(h)$ against h increased rapidly for small window sizes, as shown by the steeper slope of the line at the lower end of the x-axis, indicating a strong correlation of elevation variations at small scales. For large window sizes, $W(h)$ varied gradually.

For 20 % and 12 % slope, and most of the data for 5 %, the $W(h)$ for all given scales h increased as the rainfall simulation proceeded, revealing a temporal increasing trend of local surface roughness (Fig. 5). Notable differences existed between the initial surface and the surface after the first simulation. Those differences were expected since the initial soil surface was configured smoothly with few rock protections, which allowed greater surface changes during initial rainfall applications. Once the soil surface was altered by the first rainfall event, the erosion-induced roughness then, in turn, imposed a greater resistance to erosion for the subsequent events, reducing the morphology changes during the subsequent simulations (Nearing et al., 2017). For the most part, $W(h)$ tended to be greater at all scales for each subsequent simulation for each experiment. While at 5 % slope, the $W(h)$ functions for the initial surface and the surface after the first simulation crossed at a scale between approximately 150 and 200 mm. This means that roughness at the larger scale actually decreased slightly between the initial surface and the surface after the first simulation.

Fig. 6 shows that surfaces exhibit a fractal nature over the lower portion of the scale range, as evidenced by the linear relationship between $\log(W(h))$ and $\log(h)$. The fitting line of $\log(W(h))$ against $\log(h)$ was used for calculating Hurst exponent, H , for each surface. The results that the fractal spectrum of local roughness was limited to only the lower portion of entire scale are in accordance with previous research (Huang, 1998; Huang and Bradford, 1992; Vermang et al., 2013; Vidal Vázquez et al., 2008, 2010). In other words, the fractal nature of the soil surface has scale limitations, rather than being present at all measured scales (Whalley and Orford, 1989). The fact that the soil surface had fractal properties within a limited scale range has also been defined as pseudofractal (Whalley and Orford, 1989; García-Serrana et al., 2018; Huang, 1998; Vermang et al., 2013; Chi et al., 2012). The concept of the

pseudofractal has meant that elevation variations for small scales do not scale up proportionally as the length scale increases (Huang and Bradford, 1992); and hence one fractal model is not sufficient to quantify the surface form over the entire scale range (Whalley and Orford, 1989). Since the soil surface displayed fractal behavior only within limited length scale ranges, only the surface variations of those short scale ranges were incorporated in the calculations for estimating fractal dimension, which restricts the application of fractal dimension to distinguish differences over entire scale range (i.e., the whole plot) (Vermang et al., 2013).

4.2.2. Variations of fractal dimension and crossover length over time

Fig. 7 shows the fractal dimension, D (Eq. [6]), and crossover length, L (Eq. [5]), as a function of cumulative runoff. In Figs. 4 and 5 we see that RR and $W(h)$, both indices of surface roughness (the vertical elevation variations), tended to increase as the experiment proceeded, while in Fig. 7 we see that D tended to decrease, at least after the first or second simulation. It is sometimes suggested that fractal dimension is an index of roughness, but as we see in our data, this is not strictly true. Instead, as mentioned previously, fractal dimensions characterize the extent to which the object deviates from its topological dimension space towards its embedding dimension space (Abedini and Shaghaghian, 2009; Chi et al., 2012). In that sense, the fractal dimension is a mathematical measure of how much space a particular surface function fills (Brown, 1987).

If we consider two idealized surfaces with similar “mini-roughness,” or roughness on the mm to cm scale, but one with depressions caused by rilling at the ca. 10 cm scale, for example, we can visualize what is happening here. Referring to the schematic in Fig. 8, we see the side-view of surface A, which is planer looked at across the entire length shown, but has roughness indicated as deviations from the plane. Surface B has the same deviations from the trend line across the width, but also has two depressions caused in this case (we will say) by rill formation. In this idealized case, surface B will have greater random roughness than surface A, because the standard deviation of the elevation values for surface B are greater across the full width. However, the volumes that these surfaces are “tending to fill” are different. Since z_2 is greater than z_1 , then surface B is less able to fill the volume in which it sits, hence D for surface B will be less than for surface A. We propose that this is what is happening in the experiment, explaining the converse changes in roughness and fractal dimension. More rilling occurred at 20 % slope than at 5 % (Nearing et al., 2017; Li et al., 2019a), hence more depressions caused by the rills are seen across the width of the plot for 20 % slope, and hence D was less for the 20 % slope (Fig. 7). Lower fractal dimension associated with greater RR was also reported by Chi et al. (2012) and García-Serrana et al. (2018) when the deeper “rills” or “depressions” existed on the surfaces.

Fig. 7 shows that L consistently increased over time for all slope treatments, as did the temporal trends of the RR index (Fig. 4). However, there is qualitative difference between the final values of L and RR, in that final RR was different as a function slope while L for all slopes tended to a value of approximately $h = 0.8\text{--}1$ mm. Theoretically, the value of L represents that in which $W(L) = L$, where the local RMS roughness is equal to the scale. However, we also note that this value is much less than the values of h for scales that we actually calculated, which was a minimum of 20 mm. This can be visualized in Fig. 6 as the extrapolation from the data points to the crossover points at the 1:1 line. Basically, the L value is providing scale to the relationships, in the sense that it identifies the relative position of the lines on the graphs in Fig. 6. It was worth noting that the variability of fractal dimension among six replications was relatively small, while the values of crossover length displayed much greater differences (Fig. 7). One example is replication 2 on 20 % slope, as shown in the Fig. 6, the slopes of $\log(W(h))$ vs. $\log(h)$ were approximately the same, while the intercepts on the 1:1 line displayed apparent differences. It has been previously reported that crossover length was more sensitive to changes in

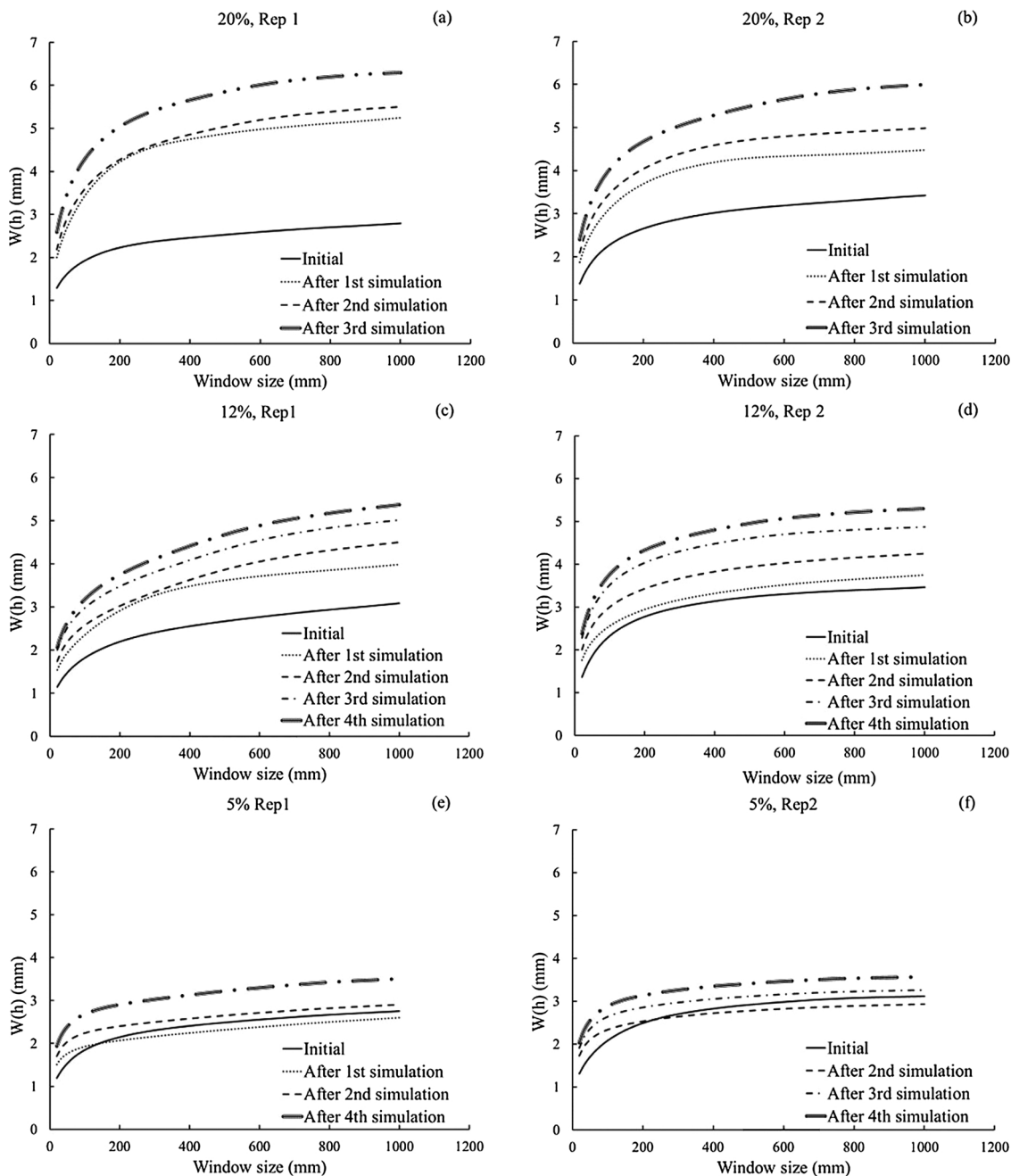


Fig. 5. The relationship between the local RMS roughness, $W(h)$, and window size, h , for each experiment.

microtopography than was fractal D (García-Serrana et al., 2018; Huang, 1998; Paz Ferreiro et al., 2008).

From the analyses above we showed that both random roughness and crossover length are indicators of surface roughness, and the difference between them is one of scale. Crossover length is a measure of roughness at a fine scale, in our case on the order of a few millimeters. Random roughness, on the other hand, is a measure of elevation variation on the scale of the length of the transect measured, which in our case was of the order of 1.5 m, thus it will include larger morphological features such as rills. This would seem to have apparent importance when characterizing flow velocities on the surface at different scales. The fractal dimension, however, is not necessarily related to the roughness magnitude, but the form of the soil surface, which has importance in the understanding of

overland flow generation processes, such as the depressional storage and hydrological connectivity (Chi et al., 2012).

4.3. Multifractal analysis

4.3.1. Generalized fractal dimension $D(q)$

Fig. 9 shows one example of the fitting results of $D(q)$. As indicated in the graph, the slope was negative when $q < 0$ while positive when $q > 0$. There were no points that noticeably departed from the straight line. All the coefficients of determination of the fitted lines were greater than 0.999, indicating strong multiple fractal behaviors (Luo et al., 2017; Martínez et al., 2009).

Fig. 10 shows the generalized fractal dimension $D(q)$, of surfaces in

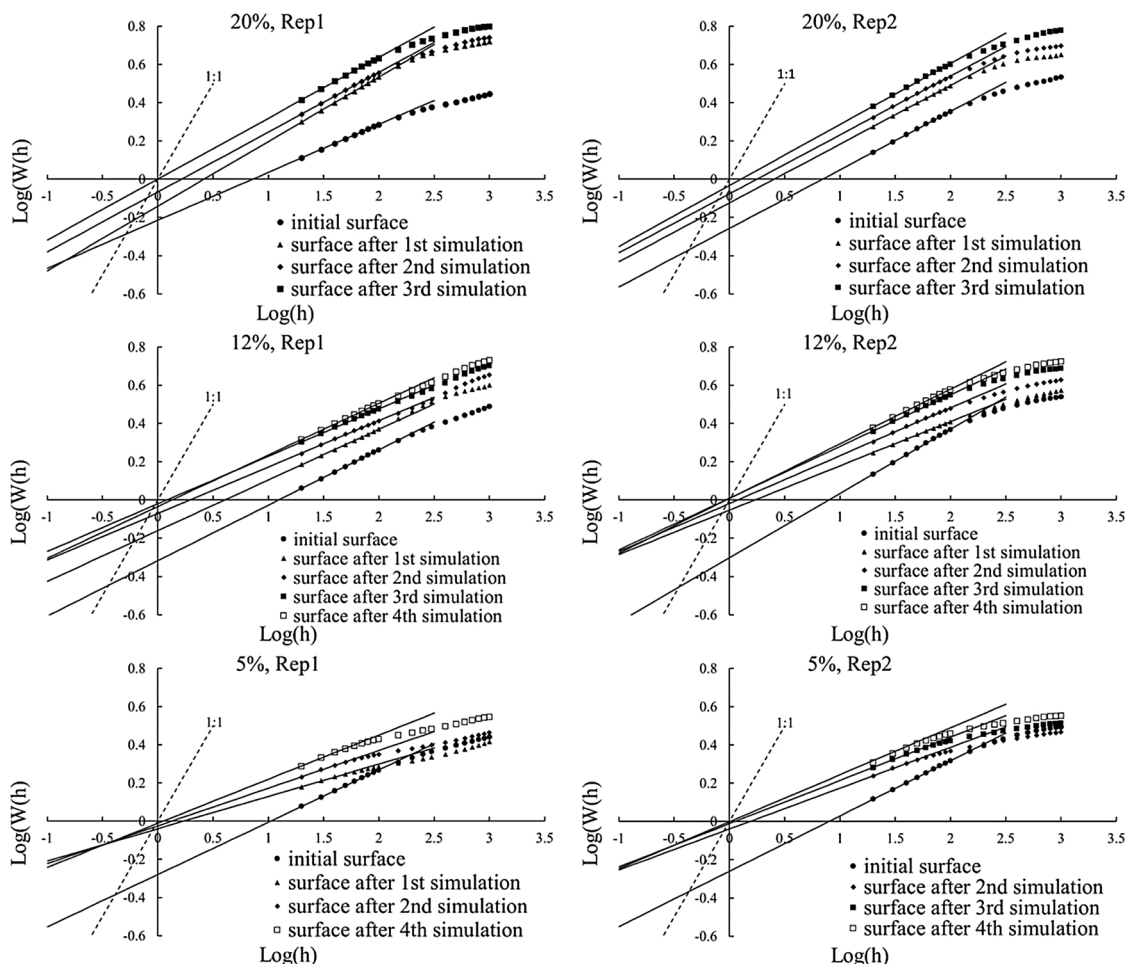


Fig. 6. The log-log relationship between the local RMS roughness, $W(h)$, and window size, h , for each experiment. Note that, for clarity, not all computed points for greater than approximately $\text{log}(h) = 2$ are plotted.

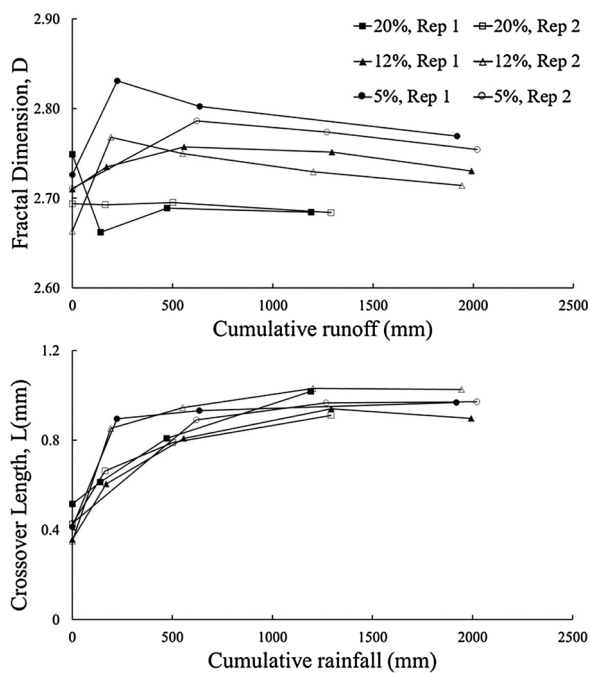


Fig. 7. The fractal dimension and crossover length for each surface as functions of cumulative runoff for each slope replication.

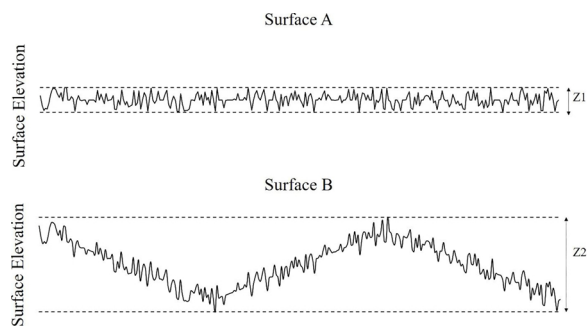


Fig. 8. Schematic diagram comparing hypothetical surfaces without (A) and with (B) idealized rills.

replication 1 of 20 % during successive rainfalls, as an example. One benefit of looking at a range of different weighting factors was to distinguish the nature of the surface spatial variations more easily. Referring to Eq. [8], we see that for $q > 0$, greater values of the normalized standard deviations, $\mu_j(h)$, are weighted when calculating values of χ , while the lesser values of deviation are weighted when $q < 0$. As such, q may act as a scanning tool to identify the existence of singularity, or extreme high and low, regions of the $\mu_j(h)$ (Martínez et al., 2009). In general, as q increases $D(q)$ will become progressively less since both $1/(q-1)$ and $\ln(\chi)$ decrease (see Eq. [9] and [10]), which is indicated in Fig. 10.

Note that if there is no singularity or variation in elevation, which means $\mu_j(h)$ is identical for all the cells, the surface then displays as

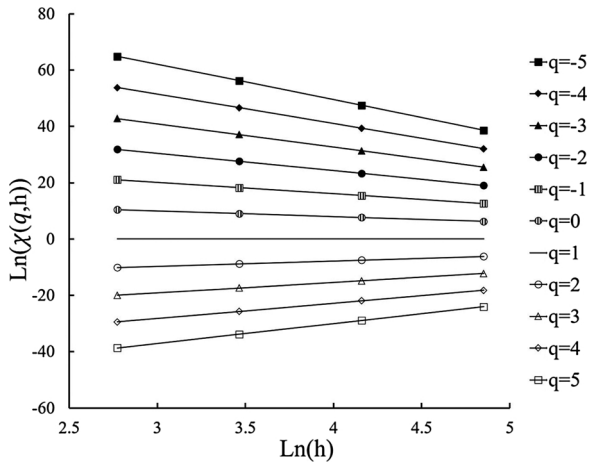


Fig. 9. Relationship between $\ln(\chi(q, h))$ and $\ln(h)$ from the surface in replication 1 on 20 % slope after the third simulation.

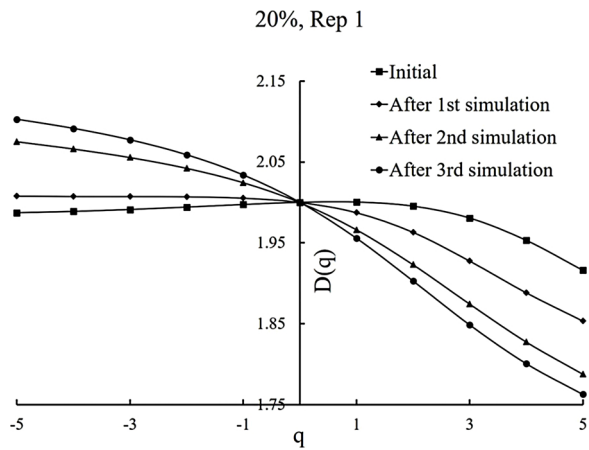


Fig. 10. Generalized fractal dimension, $D(q)$, as a function of the weighting factor, q , for each surface of replication 1 on 20 % slope.

monofractal because each cell is self-similar. Hence in that case, for any given q , $D(q) = \frac{1}{q-1} \lim_{h \rightarrow 0} \frac{\ln[\chi(q, h)]}{\ln(h)} = \frac{1}{q-1} \times \frac{\ln[\chi(q, h_1)] - \ln[\chi(q, h_2)]}{\ln(h_1) - \ln(h_2)} = \frac{1}{q-1} \times \frac{\ln\left(\frac{AB}{h_1^2} \times \frac{h_2^{2q}}{AB}\right) - \ln\left(\frac{AB}{h_2^2} \times \frac{h_1^{2q}}{AB}\right)}{\ln(h_1) - \ln(h_2)} = \frac{1}{q-1} \times \frac{2(q-1) \times (\ln(h_1) - \ln(h_2))}{\ln(h_1) - \ln(h_2)} = 2$. If $D(q)$ has a constant value as q changes, the surface at that range of scales is monofractal or no-fractal. For all surfaces showed in Fig. 10, the $D(q)$ functions were not linear, implying multifractal characteristics. For the $D(q)$ function of initial surface, the portion of $q < 0$ approximated the constant value of 2, which indicates few areas of low surface variations, but for $q > 0$, the $D(q)$ function was slightly concave down, showing the existences of a few areas with high surface variations, as discussed above. This would be probably due to the existence of a few randomly located rocks resting above the initial surface.

4.3.2. Parameters from MFA

The capacity dimension $D(0)$, information dimension $D(1)$, width parameter ΔD , and multifractality index MI were calculated for assessing the degree of heterogeneity of soil surface roughness (Fig. 11).

For all surfaces, the capacity dimension $D(0)$ was 2.000, which equaled to the theoretical value of 2, indicating that every cell was occupied. Since capacity dimension only accounted for whether the cell was occupied or not regardless of the value or distribution of each cell, no information about the soil surface heterogeneity was available using capacity dimension $D(0)$.

All reported values of $D(1)$ were less than $D(0)$. This is expected

since generalized fractal dimension $D(q)$ decreases as q increases. Vidal Vázquez et al. (2008) also claimed that if a soil surface has a tendency to multifractality it will be observed that $D(0) > D(1)$, and the more approximate $D(1)$ is to $D(0)$, the more homogeneous the surface roughness is. As rainfall proceeded, $D(1)$ for each replication displayed a decreasing trend, with more difference between $D(1)$ and $D(0)$, indicating the increase of surface heterogeneity. The final $D(1)$ values of 20 % had a greater difference with $D(0)$ than did those of 12 % and 5 % slopes, indicating greater surface roughness heterogeneity.

The predominant trends of ΔD , calculated as $\Delta D = D(q = -5) - D(q = +5)$, displayed an increasing trend over the rainfall applications. As discussed above, q acts as a scanning tool to identify the existence of singularity regions of $\mu_f(h)$. ΔD reflects the contrast degrees of $\mu_f(h)$, such that the greater ΔD is, the greater heterogeneity the soil surface roughness exhibits, therefore, the increasing trends of ΔD implied increased heterogeneity with cumulative rainfall. The final ΔD values of 20 % slope were greater than those of 12 % and 5 % slope, representing again greater surface roughness heterogeneity on 20 % slope.

The MI, which was calculated as $MI = -\Delta(D(0) - D(2))$, displayed a generally decreasing trend over cumulative rainfall. The final MI values were less on 20 %, followed by 12 % and then 5 % slope. The lower MI is, the more heterogeneous the surface roughness is (Vidal Vázquez et al., 2008). MI actually is another type of ΔD , the difference in our case was that $q = +5$ and $q = -5$ was used for ΔD while $q = +2$ and $q = 0$ was used for MI. The reason for putting forward MI is to minimize the errors of the linear fitting process (Vidal Vázquez et al., 2008). Since the estimate of $D(q)$ relies on the fitting quality of a log-log plot of $\chi(q, h)$ versus h , the uncertainty of the fitting process affects the final interpretation of the parameters determined from $D(q)$. For example, ΔD decreased after the first simulation of replication 1 on 20 % slope, which could be regarded as decreased heterogeneity, while an increased heterogeneity was captured by $D(1)$ and the MI. That was possibly due to the uncertainty in the estimation of generalized dimension function $D(q)$, and that the uncertainty increased as the magnitude of q increased, since the partition function, $\chi(q, h)$ is a power function of q , leading to amplified errors in ΔD . Hence, MI is considered as the best index in terms of minimum errors (Vidal Vázquez et al., 2008). Based on the MI, the steeper surface evolved to a greater SSR heterogeneity degree, which also supported the findings of Nearing et al. (2005).

4.4. The implications of this study

Unlike previous studies wherein SSR was mainly quantified based on the LiDAR-interpolated DEMs, all roughness indices in the present study were calculated based on the LiDAR point cloud directly without interpolations. The reason being here is that LiDAR-interpolated DEMs underestimated SSR due to the errors and information loss during interpolating processes, and would mislead the interpretations of temporal SSR variations (Li et al., 2019b). Our study therefore provided guidelines here for calculating multiple roughness indices using LiDAR points directly. For example, we created a new method to calculate the probability value of each cell for the multifractal analyses by normalizing the local roughness of each cell (Eq. [7]), rather than normalizing the elevations. The reason here was the fact that the number of elevation measurements of each cell spatially differed in a LiDAR point cloud while it was constant when DEMs were utilized. Otherwise, the density of elevation measurements would affect the estimation of probability values. An example is shown in the Supplement to illustrate those effects. It was also noted that the random roughness index was calculated based on a band with a width of 2 mm rather than a row of elevation measurements of interpolated DEMs (Li et al., 2019b).

SSR in the present study exhibited an increasing trend as rainfall simulation progressed, which is not in agreement with those studies in which agricultural soil was used and decreasing trends of SSR overtime were reported. Those differences were because in our experiments rock cover accumulated and erosional-features developed around rock

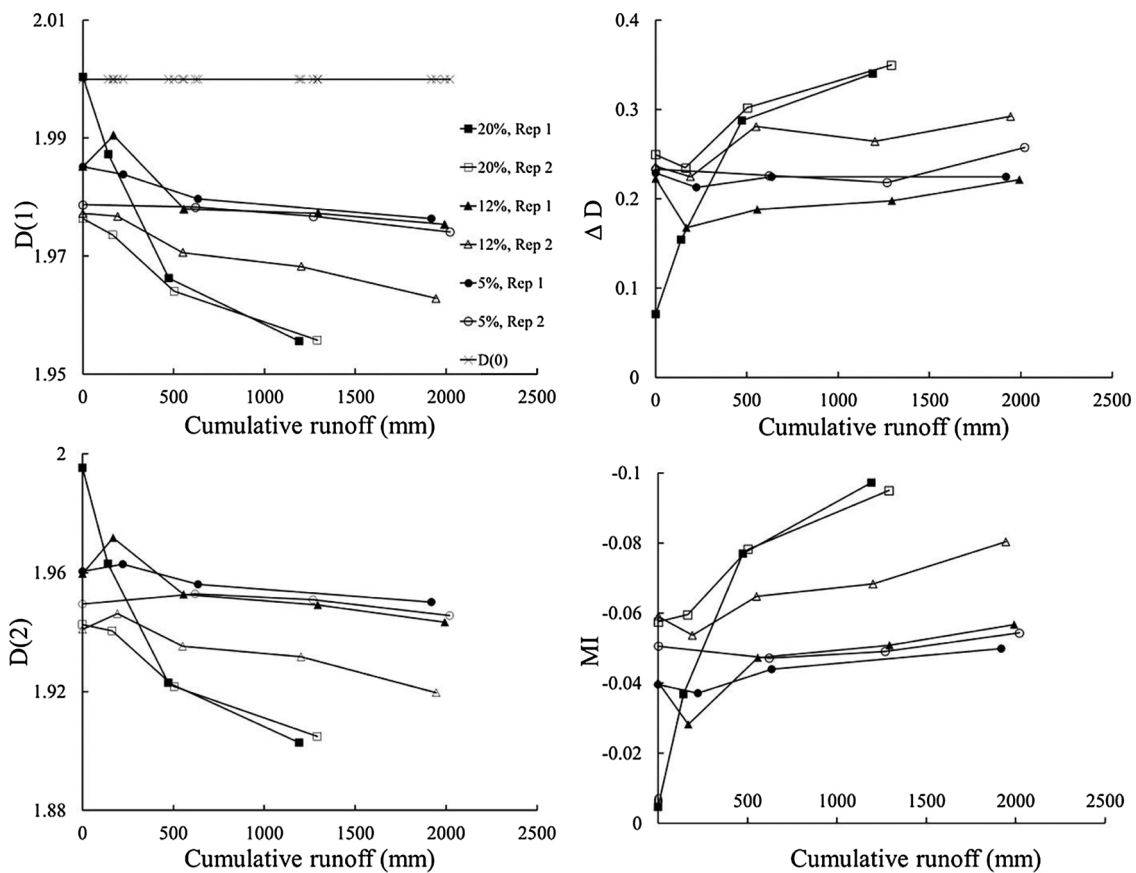


Fig. 11. The capacity dimension $D(0)$, entropy dimension $D(1)$, correlation dimension $D(2)$, width parameter ΔD and multifractality index MI as functions of cumulative runoff. Note the y-axis on the graph of MI , where up indicates greater magnitudes of negative values.

fragments that enhanced the SSR, while agricultural soil generally experiences breakdown of aggregates and subsequent sealing of the surface that smooths the surfaces. The results in this study imply that hillslopes in semi-arid landscapes can evolve in a way such that surface roughness is increased through soil erosion (Nearing et al., 2017).

Steeper slopes produced greater SSR, which was indicated by three SSR indices. This result has significant implications for understanding the dynamic feedback mechanism between erosion, surface morphology and hydraulics, that as erosion pavement develops, greater physical roughness that formed on the steeper slopes through the preferential erosion has the potential to counteract the greater component of the gravity force vector in the downslope direction on steeper slopes, resulting a more uniform erosion rate and flow velocity over widely differing hillslope gradients (our unpublished data) (Nearing et al., 2005, 2017). This feedback between erosion and surface morphology might explain the previous findings at the watershed scale that hillslope gradients may be, in certain circumstances, decoupled from erosion rates (Riebe et al., 2000; Nearing et al., 2005).

5. Conclusions

The present study investigated the surface roughness evolution of stony plots with the aid of LiDAR. Our results showed that the steeper slope evolved to greater surface roughness and SSR heterogeneity as quantified by RR, fractal dimension and the crossover length, and multifractal analysis. The increased irregularity and roughness over rainfalls was resultant from both the cumulative rock cover increase due to the selective erosion, and the formation of erosional features, e.g., rills and depressions.

Roughness indices were calculated from LiDAR points directly for avoiding the uncertainties of LiDAR-interpolated DEMs. The RR index

was shown to be a good estimator in discriminating roughness level of given rain sequence. Fractal analysis was also conducted to tackle the drawbacks of RR that neglect the spatial correlation of roughness elements. Fractal dimension and crossover length provided supplementary information about the spatial organization of the roughness elements. In order to investigate the entire soil surface complexity, multiple fractal analysis (MFA), with a new probability function that designed for LiDAR points, was also conducted. The parameters derived from MFA, especially the MI , enabled us to provide quantitative measures of SSR heterogeneity. Compared with single fractal analysis, MFA better characterized the surface complexity for entire scale and required less computation effort, which is important for highly dense measurements (e.g., LiDAR). Further research should focus on relating the parameters from MFA with water flow hydraulics in order to incorporate these parameters into erosion models.

Declaration of Competing Interest

This research did not receive any specific grant from funding agencies in the public, commercial, or not-for-profit sectors.

Competing interests. The authors declare that they have no conflict of interest.

Acknowledgements

We thank John Smith for the soil box preparation and soil collection. The Southwest Watershed Research Center hosted a number of workshops.

References

- Abban, B.K.B., Papanicolaou, A.N.T., Giannopoulos, C.P., Dermisis, D.C., Wacha, K.M., Wilson, C.G., Elhakeem, M., 2017. Quantifying the changes of soil surface micro-roughness due to rainfall-induced erosion on a smooth surface. *Nonlinear Process. Geophys. Discuss.* 1–20. <https://doi.org/10.5194/npg-2016-76>.
- Abedini, M.J., Shaghaghian, M.R., 2009. Exploring scaling laws in surface topography. *Chaos Solitons Fractals* 42, 2373–2383. <https://doi.org/10.1016/j.chaos.2009.03.121>.
- Abrahams, A.D., Parsons, A.J., Wainwright, J., 1994. Resistance to overland flow on semiarid grassland and shrubland hillslopes, Walnut Gulch, southern Arizona. *J. Hydrol.* 156, 431–446. [https://doi.org/10.1016/0022-1694\(94\)90088-4](https://doi.org/10.1016/0022-1694(94)90088-4).
- Allmaras, R.R., Burwell, R.E., Larson, W.E., Holt, R.F., 1966. Total Porosity and Random Roughness of the Intertow Zone As Influenced by Tillage. Conservation Research Report No. 7. U S Department of Agriculture, Washington, USA.
- Bauer, T., Strauss, P., Grims, M., Kampfner, E., Mansberger, R., Spiegel, H., 2015. Long-term agricultural management effects on surface roughness and consolidation of soils. *Soil Tillage Res.* 151, 28–38. <https://doi.org/10.1016/j.still.2015.01.017>.
- Besl, P., McKay, N., 1992. A method for registration of 3-D shapes. *IEEE Trans. Pattern Anal. Mach. Intell.* <https://doi.org/10.1109/34.121791>.
- Brown, S.R., 1987. A note on the description of surface roughness using fractal dimension. *Geophys. Res. Lett.* 14, 1095–1098. <https://doi.org/10.1029/GL014i011p01095>.
- Chi, Y., Yang, J., Bogart, D., Chu, X., 2012. Fractal analysis of surface microtopography and its application in understanding hydrologic processes. *Trans. ASABE* 55, 1781–1792. <https://doi.org/10.13031/2013.42370>.
- Currence, H.D., Lovely, W.G., 1970. Analysis of soil surface roughness. *Trans. Am. Soc. Agric. Eng.* 13, 710–714. <https://doi.org/10.13031/2013.38702>.
- Darboux, F., Davy, P., Gascuel-Oudoux, C., Huang, C., 2001. Evolution of soil surface roughness and flowpath connectivity in overland flow experiments. *Catena* 46, 125–139.
- Ding, W., Huang, C., 2017. Effects of soil surface roughness on interrill erosion processes and sediment particle size distribution. *Geomorphology* 295, 801–810. <https://doi.org/10.1016/j.geomorph.2017.08.033>.
- García-Serrana, M., Gulliver, J.S., Nieber, J.L., 2018. Description of soil micro-topography and fractional wetted area under runoff using fractal dimensions. *Earth Surf. Process. Landforms* 43, 2685–2697. <https://doi.org/10.1002/esp.4424>.
- Gneiting, T., Schlather, M., 2004. Stochastic models that separate fractal dimension and the Hurst effect. *SIAM Rev. Soc. Ind. Appl. Math.* 46, 269–282. <https://doi.org/10.1137/S0036144501394387>.
- Gómez, J.A., Nearing, M.A., 2005. Runoff and sediment losses from rough and smooth soil surfaces in a laboratory experiment. *Catena* 59, 253–266. <https://doi.org/10.1016/j.catena.2004.09.008>.
- Govers, G., 1992. Relationship between discharge, velocity and flow area for rills eroding loose, non-layered materials. *Earth Surf. Process. Landforms* 17, 515–528. <https://doi.org/10.1002/esp.3290170510>.
- Govers, G., Takken, I., Helming, K., 2000. Soil roughness and overland flow. *Agronomie* 20, 131–146. <https://doi.org/10.1051/agro:2000114>.
- Helming, K., Roth, C.H., Wolf, R., Diestel, H., 1993. Characterization of rainfall - microrelief interactions with runoff using parameters derived from digital elevation models (DEMs). *Soil Technol.* 6, 273–286. [https://doi.org/10.1016/0933-3630\(93\)90016-8](https://doi.org/10.1016/0933-3630(93)90016-8).
- Huang, C., 1998. Quantification of soil microtopography and surface roughness. In: Baveye, P., Parlange, J.Y., Stewart, B.A.E. (Eds.), *Fractals in Soil Science*. CRC Press, Boca Raton, FL, USA, pp. 153–168.
- Huang, C., Bradford, J., 1992. Applications of a laser scanner to quantify soil microtopography. *Soil Sci. Soc. Am. J.* 56, 14–21. <https://doi.org/10.2136/sssaj1992.03615995005600010002x>.
- Huihui, Z., Na, T., Qingfeng, Z., 2016. Spatial heterogeneity of loess contour tilled microtopographic slope in rainfall erosion. *Soil Sci. Plant Nutr.* 62, 409–415. <https://doi.org/10.1080/00380768.2016.1218742>.
- Kamphorst, E.C., Jetten, V., Guerif, J., Pitkanen, J., Iversen, B.V., Douglas, J.T., Paz, A., 2000. Predicting depression storage from soil surface roughness. *Soil Sci. Soc. Am. J.* 64, 1749. <https://doi.org/10.2136/sssaj2000.6451749x>.
- Lei, T., Nearing, M.A., Haghighi, K., Bralts, V.F., 1998. Rill erosion and morphological evolution: a simulation model. *Water Resour. Res.* 34, 3157–3168. <https://doi.org/10.1029/98WR02162>.
- Li, L., Nearing, M.A., Nichols, M.H., Polyakov, V.O., Cavanaugh, M.L., 2019a. Using terrestrial LiDAR to measure water erosion on stony plots under simulated rainfall. Accepted by *J. Earth Surf. Processes Landforms*.
- Li, L., Nearing, M.A., Nichols, M.H., Polyakov, V.O., Cavanaugh, M.L., 2019b. The effects of DEM interpolation on quantifying soil surface roughness using terrestrial LiDAR. Accepted by *Soil Tillage Res.*
- Lopes, R., Betrouni, N., 2009. Fractal and multifractal analysis: a review. *Med. Image Anal.* 13, 634–649. <https://doi.org/10.1016/j.media.2009.05.003>.
- Luo, J., Zheng, Z., Li, T., He, S., 2017. Spatial heterogeneity of microtopography and its influence on the flow convergence of slopes under different rainfall patterns. *J. Hydrol.* 545, 88–99. <https://doi.org/10.1016/j.jhydrol.2016.12.018>.
- Malinverno, A., 1990. A simple method to estimate the fractal dimension of a self-affine series. *Geophys. Res. Lett.* 17, 1953–1956. <https://doi.org/10.1029/GL017i011p01953>.
- Martínez, F.S.J., Caniego, J., Guber, A., Pachepsky, Y., Reyes, M., 2009. Multifractal modeling of soil microtopography with multiple transects data. *Ecol. Complex.* 6, 240–245. <https://doi.org/10.1016/j.ecocom.2009.05.002>.
- Moreno, R.G., Álvarez, M.C.D., Alonso, A.T., Barrington, S., Requejo, A.S., 2008a. Tillage and soil type effects on soil surface roughness at semiarid climatic conditions. *Soil Tillage Res.* 98, 35–44. <https://doi.org/10.1016/j.still.2007.10.006>.
- Moreno, R.G., Alvarez, M.C.D., Requejo, A.S., Tarquis, A.M., 2008b. Multifractal analysis of soil surface roughness. *Vadose Zone J.* 7, 512. <https://doi.org/10.2136/vzj2007.0016>.
- Nearing, M.A., Kimoto, A., Nichols, M.H., Ritchie, J.C., 2005. Spatial patterns of soil erosion and deposition in two small, semiarid watersheds. *J. Geophys. Res. Earth Surf.* 110, 1–11. <https://doi.org/10.1029/2005JF000290>.
- Nearing, M.A., Nichols, M.H., Stone, J.J., Renard, K.G., Simanton, J.R., 2007. Sediment yields from unit-source semiarid watersheds at Walnut Gulch. *Water Resour. Res.* 43, 1–10. <https://doi.org/10.1029/2006WR005692>.
- Nearing, M.A., Polyakov, V.O., Nichols, M.H., Hernandez, M., Li, L., Zhao, Y., Armendariz, G., 2017. Slope-velocity equilibrium and evolution of surface roughness on a stony hillslope. *Hydrol. Earth Syst. Sci. Discuss.* 21, 3221–3229. <https://doi.org/10.5194/hess-21-3221-2017>.
- Nouwakpo, S.K., Weltz, M.A., McGwire, K., 2016. Assessing the performance of structure-from-motion photogrammetry and terrestrial LiDAR for reconstructing soil surface microtopography of naturally vegetated plots. *Earth Surf. Process. Landforms* 41, 308–322. <https://doi.org/10.1002/esp.3787>.
- Paige, G.B., Stone, J.J., Smith, J.R., Kennedy, J.R., Joel Stone, J., Richard Smith, J., Hydrologic Technician, S., Ronald Kennedy, J., Paige, G., 2003. The walnut gulch rainfall simulator: a computer-controlled variable intensity rainfall simulator. *Appl. Eng. Agric.* 20, 25–31.
- Paz Ferreira, J., Bertol, I., Vidal Vázquez, E., 2008. Quantification of tillage, plant cover, and cumulative rainfall effects on soil surface microrelief by statistical, geostatistical and fractal indices. *Nonlinear Process. Geophys.* 15, 575–590. <https://doi.org/10.5194/npg-15-575-2008>.
- Polyakov, V., Nearing, M.A., Stone, J., 2018. Velocities of shallow overland flow on semiarid hillslopes. *Earth Surface Processes and Landforms* 43 (12), 2578–2583.
- Renard, K.G., Nichols, M.H., Woolhiser, D.A., Osborn, H.B., 2008. A brief background on the U.S. department of agriculture agricultural research service walnut gulch experimental watershed. *Water Resour. Res.* 44, 1–11. <https://doi.org/10.1029/2006WR005691>.
- Riebe, C.S., Kirchner, J.W., Granger, D.E., Finkel, R.C., 2000. Erosional equilibrium and disequilibrium in the Sierra Nevada, inferred from cosmogenic ²⁶Al and ¹⁰Be in alluvial sediment. *Geology* 28 (9), 803.
- Riegl GmbH, 2012. LAS Extrabytes Implementation in RIEGL Software 2012.
- Roisin, C.J.C., 2007. A multifractal approach for assessing the structural state of tilled soils. *Soil Sci. Soc. Am. J.* 71, 15. <https://doi.org/10.2136/sssaj2006.0132>.
- Römkens, M.J.M., Wang, J.Y., 1986. Effect of tillage on surface roughness. *Trans. Am. Soc. Agric. Eng.* 29, 429–433.
- Salat, H., Murcio, R., Arcaute, E., 2017. Multifractal methodology. *Phys. A Stat. Mech. Int. Appl.* 473, 467–487. <https://doi.org/10.1016/j.physa.2017.01.041>.
- Shaw, C.F., 1929. Erosion pavement. *Geogr. Rev.* 19, 638–641.
- Van Wesemael, B., Poesen, J., De Figueiredo, T., Covers, G., 1996. Surface roughness evolution of soils containing rock fragments. *Earth Surf. Process. Landforms* 21, 399–411. [https://doi.org/10.1002/\(SICI\)1096-9837\(199605\)21:5<399::AID-ESP567>3.0.CO;2-M](https://doi.org/10.1002/(SICI)1096-9837(199605)21:5<399::AID-ESP567>3.0.CO;2-M).
- Vermang, J., Norton, L.D., Baetens, J.M., Huang, C., Cornelis, W.M., Gabriels, D., 2013. Quantification of soil surface roughness evolution under simulated rainfall. *Trans. ASABE* 56, 505–514. <https://doi.org/10.13031/2013.42670>.
- Vermang, J., Norton, L.D., Huang, C., Cornelis, W.M., da Silva, A.M., Gabriels, D., 2015. Characterization of soil surface roughness effects on runoff and soil Erosion rates under simulated rainfall. *Soil Sci. Soc. Am. J.* 79, 903–916. <https://doi.org/10.2136/sssaj2014.08.0329>.
- Vidal Vázquez, E., Vivas Miranda, J.G., Paz González, A., 2005. Characterizing anisotropy and heterogeneity of soil surface microtopography using fractal models. *Ecol. Modell.* 182, 337–353. <https://doi.org/10.1016/j.ecolmodel.2004.04.012>.
- Vidal Vázquez, E., Miranda, J.G.V., Alves, M.C., Paz González, A., 2006. Effect of tillage on fractal indices describing soil surface microrelief of a Brazilian Alfisol. *Geoderma* 134, 428–439. <https://doi.org/10.1016/j.geoderma.2006.03.012>.
- Vidal Vázquez, E., García Moreno, R., Miranda, J.G.V., Díaz, M.C., Saá Requejo, A., Paz Ferreira, J., Tarquis, A.M., 2008. Assessing soil surface roughness decay during simulated rainfall by multifractal analysis. *Nonlinear Process. Geophys.* 15, 457–468. <https://doi.org/10.5194/npg-15-457-2008>.
- Vidal Vázquez, E., Miranda, J.G.V., Paz Ferreira, J., 2010. A multifractal approach to characterize cumulative rainfall and tillage effects on soil surface microtopography and to predict depression storage. *Biogeosciences* 7, 2989–3004. <https://doi.org/10.5194/bg-7-2989-2010>.
- Whalley, W.B., Orford, J.D., 1989. The use of fractals and pseudofractals in the analysis of two-dimensional outlines: review and further exploration. *Comput. Geosci.* 15, 185–197. [https://doi.org/10.1016/0098-3004\(89\)90033-2](https://doi.org/10.1016/0098-3004(89)90033-2).
- Willgoose, G.R., Sharmeen, S., 2006. A one-dimensional model for simulating armouring and erosion on hillslopes: 1. Model development and event-scale dynamics. *Earth Surf. Process. Landforms* 31, 970–991. <https://doi.org/10.1002/esp.1398>.
- Wong, P., 1987. Fractal surfaces in porous media. *AIP Conference Proceedings* 304–317. <https://doi.org/10.1063/1.36383>.
- Zhao, L., Huang, C., Wu, F., 2016. Effect of microrelief on water erosion and their changes during rainfall. *Earth Surf. Process. Landforms* 41, 579–586. <https://doi.org/10.1002/esp.3844>.